RSC Advances

ROYAL SOCIETY OF CHEMISTRY

www.rsc.org/advances

Influence of surfactant alkyl length in functionalizing sol-gel derived microporous cobalt oxide silica

Gianni Olguin[1,2], Christelle Yacou[1], Simon Smart[1,*], João C. Diniz da Costa[1]

[1]The University of Queensland, FIMLab - Films and Inorganic Membrane Laboratory, School of Chemical Engineering, Brisbane, Qld, 4072, Australia

[2]Pontificia Universidad Católica de Valparaíso, Escuela de Ingeniería Química, Valparaíso, Chile

(*) corresponding author (s.smart@uq.edu.au)

Abstract

The size or alkyl chain length of cationic surfactants can be used to tailor both the pore morphology and the functionality or oxidation state of cobalt in silica materials. This work shows for the first time that these two mechanisms are interconnected. Cobalt oxide silica materials, with the same cobalt loading (Co:Si = 1:4), were prepared using an acid catalysed sol-gel method where the cobalt/surfactant ratio was systematically varied. The alkyl chain length of the cationic surfactant was also varied from 2 to 12 by using tetraethyl (C2-AB) ammonium bromide, and triethyl hexyl (C6-AB) and dodecyl trimethyl (C12-AB) ammonium bromides as the templating agents. Initial addition of C2-AB, C6-AB or C12-AB enhanced the oxidation of cobalt to cobalt (II,III) oxide in the xerogels. However, as more surfactant is added the enhancement effect is reversed and the cobalt (II,III) oxide content of the sample begins to decline. The point at which this transition occurs is a function of the alkyl chain length of the surfactant, with a longer chain indicating an earlier transition. Pore

morphology was influenced in a similar fashion with the longer alkyl chain C12-AB surfactant undergoing an earlier transition (i.e. at lower concentrations) towards mesoporosity, than either of the smaller C2-AB and C6-AB surfactants. In both mechanisms it was the increased propensity of the C12-AB surfactant to aggregate (given its larger size and lower solubility) that was the controlling factor.

Key words: Silica, Sol-gel, Cobalt, Surfactant, Halide

Introduction

Cobalt oxide containing silica has become one of the preferred functional materials for a broad range of applications. Molecular sieves,[1-3] catalysts,[4] magnetic materials and gas sensors,[5,6] for instance, have shown significant improvements over the last decades. Likewise, the evolution of pore size tailoring and structure direction in silica through the templating process has led to enhanced functionality in both micro and mesoporous silica.[7-9] These complementary techniques have been strengthened by the adoption and development of sol-gel methods, promoting a more controlled and less complex preparation pathway.[6,10] However, the synergetic effect of employing these two techniques simultaneously in sol-gel based silica has yet to be explored and not well understood.

The silica sol-gel combined incorporation of cobalt and organic templates has been mainly reported for mesoporous materials, preferentially on minor cobalt dosage (< 10 %wt.) and quaternary ammonium surfactants as template agents. Several studies focused on MCM 41 pore change as a function of the surfactant alkyl lengths only,[11] or the reduction of surface area by using hexadecyl ammonium bromide (C16-AB) derived MCM 41 and 48 materials under cobalt load,[12,13] or template decomposition effects.[14,15] A common feature of all these reports in the literature is the lack of evaluation of the counter effect of the template agent on the embedded cobalt in the silica matrix.

Recently, it was unveiled by Olguin and co-workers[16] that there is a significant interaction between cobalt oxide and cationic surfactants in silica sol-gel method. By using a short cationic surfactant hexyl triethyl ammonium bromide (C6-AB), this group reported for the first time that the metal oxidation was substantially modified as a function of the template agent. For instance, a low surfactant load led to an increase in the cobalt (II,III) oxide phase formation whilst the opposite effect occurred with excess surfactant content. Coordination of cobalt with the surfactant's bromine counter-ion was highly favourably during the non-aqueous sol-gel process and was identified as principle mechanism promoting the altered oxidation state of cobalt after thermal treatment. However, this novel study was limited to a single cationic surfactant, and the overall effect of the length of the alkyl chains in structural formation concomitant with the cobalt oxidation state is not known. Thus, understanding how the cobalt incorporation is affected by surfactant templating provides a different approach to enhance the current knowledge about the synergy of these two functionalization techniques.

Here we show that that the length of the alkyl chain has a more significant role in both structural and metal oxidation formation than previously thought. To investigate this combined functionalization effect, we used a quaternary ammonium surfactant series based on tetraethyl (C2-AB) ammonium bromide, and hexyl triethyl (C6-AB) and dodecyl trimethyl (C12-AB) ammonium bromides as the templating agents. An acid catalysed sol-gel method is employed where the cobalt/surfactant ratio is systematically varied to determine the synergistic functionalization effect of these two additives to the silica sol. Calcined xerogels were fully characterized to determine their structures in tandem with the resultant cobalt oxidation state. A mechanistic model is proposed to explain the effect of the alkyl chain length in the synergistic functionalization of template cobalt oxide micro and mesoporous silica.

Experimental

Cobalt silica (CoSi) samples were synthesized based on a previously reported method.[17] Firstly, cobalt nitrate hexahydrate ($Co(NO_3)_2.6H_2O$) is dissolved in 30 %vol hydrogen peroxide (H_2O_2) in order to keep the pH stable around 3.0 and then diluted in an excess ethanol. Subsequently, the solution is cooled to 0 °C, followed by a slow drop-wise addition of tetraethyl orthosilicate (TEOS). The final molar ratio is $TEOS:H_2O:H_2O_2:EtOH:Co(NO_3)_2.6H_2O$ = 4 : 45.5 : 9 : 256 : 1. Lastly, the solution is moderately stirred in an ice-bath at 0 °C for three hours.

The preparation of surfactant cobalt oxide silica samples follows the same procedure, except for the addition of a cationic surfactant after the ice-bath treatment. The solubility of surfactant species was guaranteed by keeping the concentration below the critical micelle concentration (CMC) point, taking into account the surfactant type, solvent nature and counter ion presence. Samples are identified by the nomenclature CY–CoSi-X where Y represents the tail alkyl length (2, 6 or 12) and X the surfactant/cobalt molar ratio, which was varied from 0 to 2. After preparation, all sol-gel solutions were dried in an air atmosphere using an oven for 96 hours at 60 °C. The dried xerogels were then ground to a fine powder and stored in sealed containers. Subsequently, each sample was calcined at 600 °C in a furnace under air atmosphere, at a ramp rate of 1 °C min^{-1} and a dwell time of 150 min.

Calcined samples were degassed under vacuum at 200 °C for at least four hours and characterized by nitrogen gas adsorption using a Micromeritics TriStar-3000 instrument. Fourier transform infra-red (FT-IR) attenuated total reflectance (ATR) analysis was performed using a Perkin Elmer Spectrum 400 FT-IR/FT-FIR Spectrometer, over a range of 4000 to 530 cm^{-1}. FT-IR spectra were normalized using the siloxane (Si-O-Si) peak at 1040 cm^{-1} prior to deconvolution. Surface elemental compositions were obtained on a Kratos Axis ULTRA X-ray Photoelectron Spectrometer (XPS) using Al Kα X-rays (1486.6eV) at 150W (15 kV, 10 mA). High-resolution XPS spectra were charge-corrected using the C 1s peak at 284.6 eV. UV-visible (200 to 800 nm) diffuse reflectance UV-Visible (DR-UV-vis) spectra of

powdered samples were obtained on a Varian spectrophotometer equipped with an integrating sphere.

To avoid phase separated solutions and ensure homogenous integration of the surfactant into the sol-gel process, the concentration range of the various surfactants was kept such that their solubility was preserved. This was estimated through Equation 1, taking into consideration the concentration, solvent nature and ion presence in the sol.[18] The results are listed in Table 1. For example having ethanol as the main solvent, increases the critical micelle concentration threshold (CMC) when compared with aqueous solutions due to its reduced polarity.[19-21] By comparison, the presence of nitrate counter ion tends to reduce the CMC of ionic surfactants.[22,23] The final sols were homogeneous solutions for each one of the selected surfactant/cobalt ratios. An exception to this was a sol prepared with C2-AB at molar ratio X=2 where phase separation was detected.

$$CMC_{final} = CMC_{sol} \times \left(1 - \frac{cir}{100}\right)$$

Table 1: Surfactant properties.

Name	Alkyl Tail Carbon number	Formula	CMC_{water} [mM]	CMC_{sol} [mM]	*cir* [%]	CMC_{final} [mM]*
C2-AB	2	$(C_2H_5)_4NBr$	187	-	-	-
C6-AB	6	$CH_3(CH_2)_5(C_2H_5)_3NBr$	1060	>1060	20%	>1000
C12-AB	12	$CH_3(CH_2)_{11}(CH_3)_3NBr$	15.5	592	65%	207.2

*Critical Micelle Concentration of surfactants in aqueous solution (CMC_{water}) and in a mixture of 80%w ethanol and water (CMC_{sol}). Reduction of CMC due to counter ion presence is also shown (*cir*) and an estimated CMC final value (CMC_{final}) which is calculated through Equation 1.

Results

The nitrogen adsorption isotherms of xerogels made with differing concentrations of the three distinct surfactants are depicted in Figure 1. Total pore volume increases as the concentration of surfactant rises, regardless of which surfactant is used, which concurs with the increase in Brunauer-Emmett-Teller (BET) surface area (calculated per gram of sample) as is shown in Figure 1d. Both

surfactants C2-AB and C6-AB follow similar isotherm and BET surface area trends until the surfactant cobalt ratio reaches 1. This occurs despite a difference of 4 carbons in the alkyl tail length and may suggest that the tetra ethyl head group is the major influence in tailoring the pore structure, for smaller sized surfactants. Furthermore, the isotherm resembles a type I below a concentration of around 1.0, which indicates that both surfactants retain the microporous character of the silica matrix. A weak transition into type IV isotherm can be noticed with C6-AB only at high surfactant load (X=2) due to the small capillary condensation at partial pressure of above 0.4.

It is interesting to observe the role played by C12-AB in providing the largest increase in adsorption at lower concentrations, which is also observable as a steeper rise in the BET surface area (Figure 1d). From Figure 1c it can be observed that the type I isotherm is preserved until a concentration of 0.25, while further surfactant addition shifts the matrix into a predominately mesoporous structure. Despite this transition, the absence of a prominent hysteresis loop suggests a moderate shift into a lower mesoporous region, close to the micro-meso boundary. Figure 1d displays a slight decrease of BET surface area at C12-AB concentrations above 0.5 while the adsorption of nitrogen is almost constant (Figure 1c). This suggests a likely increase in pore size rather than an expansion in mesoporous volume at higher C12-AB surfactant loads.

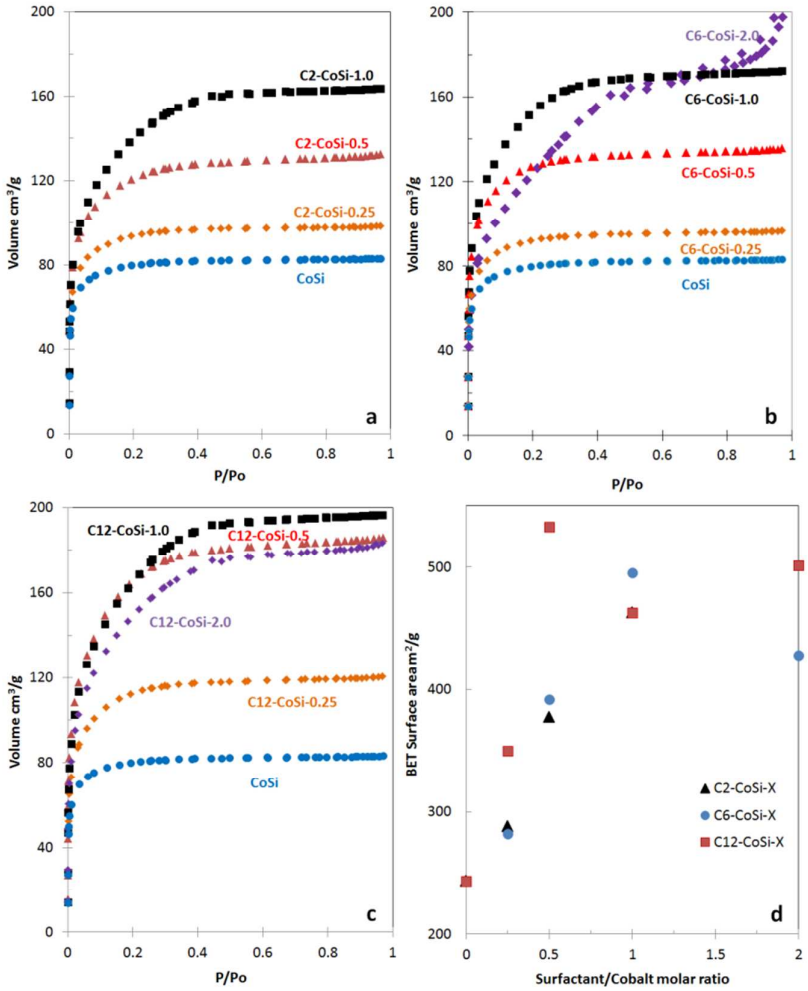

Figure 1: Nitrogen adsorption-desorption isotherms for different concentrations of surfactant a) C2-AB, b) C6-AB, c) C12-AB, d) BET surface area (m^2 per gram of total sample) as a function of surfactant concentration for each of the selected surfactants (Correlation factor higher than 0.996).

The pore size distribution of samples based on a Density Functional Theory (DFT) model is shown in Figure 2a. Standard cobalt silica as the reference material results in pore sizes generally below 2 nm, showing a tri-modal distribution between 1.2 and 2 nm. The tri-modal pore size distribution is in line with positron annihilation lifetime spectroscopy for pure microporous silica as reported by Duke and co-workers.[24] It can be also seen that surfactant incorporation induces a reduction in the amount of small pores. The smallest pore size peak almost disappears for C12-AB at X=0.5, though for the smallest surfactant C2-AB the same effect requires a high surfactant/cobalt ratio at X=1.0. This trend

concurs with the tailoring ability of these surfactants to alter pore size within the silica matrix. However, the evolving mesopore phase at high surfactant loads does not indicate a uniform tailoring process as one would expect. This lack of order may relate with a disorganized micellization process of each surfactant during sol-gel process.[25] As every initial sol was designed to keep the surfactant concentration below the CMC point (Table 1), only the early stages of aggregation or formation of proto-micelles could be expected, and even then only during the later stages of drying. [26]

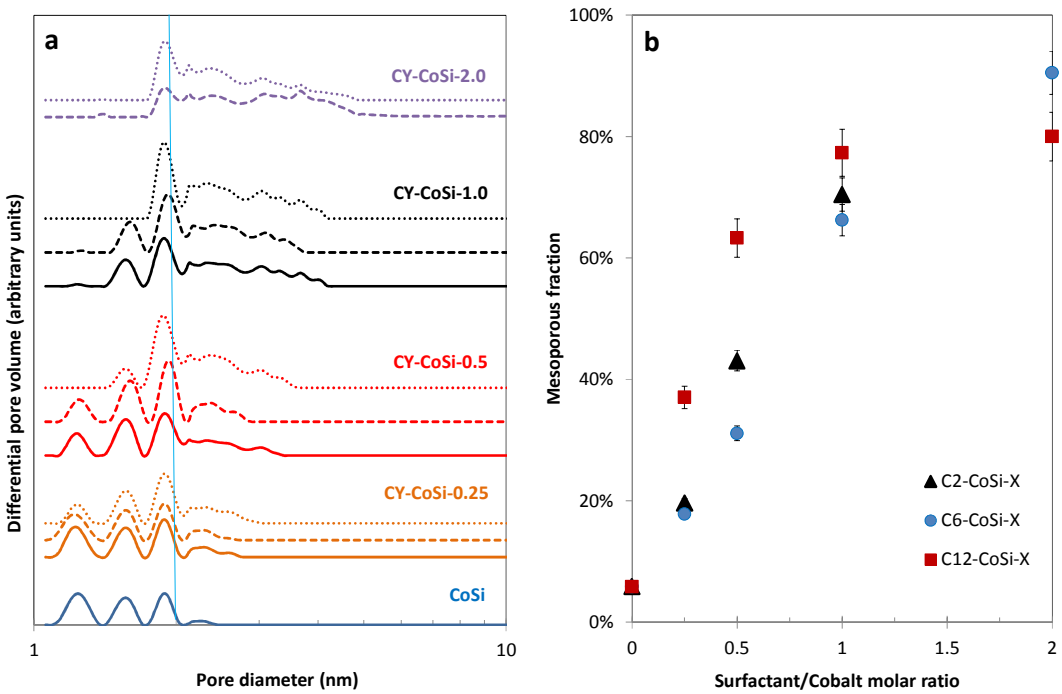

Figure 2: Pore size distribution based on DFT model for different surfactant types and concentrations. a) dV/dLog(D) graph for C2-AB: Solid line, C6-AB: dashed line, C12-AB: dotted line. Vertical blue line indicates 2 nm limit. b) Fraction of pore sizes above 2 nm. Error bars depict a 95% confidence interval.

The evolution of material mesoporosity is clearly shown in Figure 2b as a function of surfactant load. For instance, the pure cobalt oxide silica (i.e. no surfactant) produced structures with less than 6 % of pore sizes within the mesoporous region. Mesoporosity for both C2-AB and C6-AB follow a similar trend, and evolves gradually to finally become dominant at X=1 (mesopore fraction is 66%). By contrast, C12-AB undergoes a faster transition into the mesopore region (63% at X=0.5), indicating a

twofold increase in mesoporosity fraction as compared C2-AB and C6-AB cobalt oxide xerogels. There results suggest that the longer hydrophobic tail and lower CMC of C12-AB has a large influence in mesoporosity formation compared to the other smaller surfactants. This is possibly attributed to C12-AB promoting larger aggregate species and consequently a more pronounced templating effect.[27] By the same token, C2-AB and C6-AB had similar effect in the mesoporosity formation, thus indicating the alkyl tail length becomes influential only if the carbon chain is greater than 6, i.e. $C_n > C_6$.

A characterization of the cobalt species was conducted through DR-UV-vis on uncalcined materials, shown in Figure 3a. There is a clear evolution of multiple peaks at higher wavelength as the concentration of either C12-AB or C2-AB increases. These peaks above 600 nm were also evidenced with C6-AB and can be connected with the presence of $CoBr_x^{2-x}$ species in a tetrahedral coordination.[28] This species are very favourable in non-aqueous media (which is the case for our sol-gel method) and its relative abundance is affected by the Br/Co ratio. However, all the species are present in equilibrium and the related bands can be easily observed in the UV-Vis spectra. [29,30] By contrast, standard CoSi demonstrates characteristic peaks at 460 and 525 nm which is related with an octahedral coordination between the metal and active silica sites or free water molecules (Co-$(OX)_6$).[31,32] In addition, the evolution of the characteristic $CoBr_4^{-2}$ reflectance bands at 725 nm[28] is illustrated at Figure 3b as a function of surfactant load. These isolated and clearly observable bands offer a good indicator about the abundance of Co-Br complexes, despite the low concentration of the related species at low surfactant loads. It can be seen that each one of the selected surfactants follows similar evolution, despite the difference in alkyl tail length. This observation suggests a comparable formation of $CoBr_x^{2-x}$ species along the selected surfactant series and can be explained by the similar bromide proportion (molar basis) in each surfactant. Furthermore, the strong relationship depicted in Figure 3b indicates that the $CoBr_x^{2-x}$ species are preferred coordination structures rather than the traditional octahedron Co-$(OX)_6$.

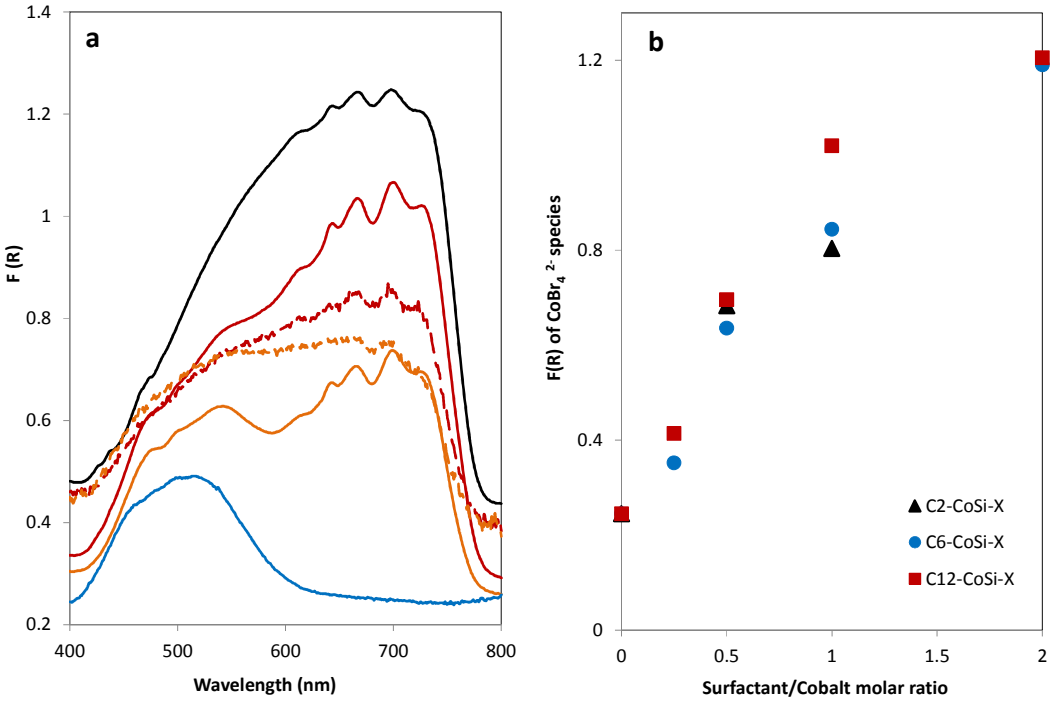

Figure 3: a) DR-UV-Vis spectra of C2-AB (dashed lines) and C12-AB (solid lines) Cobalt silica materials. b) Kubelka-Munk function values of $CoBr_4^{-2}$ species at 725 nm for different surfactant concentrations and surfactant types (despite the low likelihood of $CoBr_4$ species at low surfactant loading, the high reflectance at 725 nm offers a good indicator about the abundance of these species).

The formation of the mixed valence oxide of cobalt (Co_3O_4) in calcined xerogels was examined through FTIR and XPS. The presence of Co^{3+}-O vibration peaks at 660 cm^{-1} can be seen in almost every single IR spectrum (see supplementary Figure S1).[4] Similarly, XPS spectra of the Co 2p region provides evidence about this oxide due to the presence of a low energy peak at 779.9 eV (see supplementary Figure S2); however no other cobalt species were observed.[33,34] Figure 4a shows the evolution of FTIR intensity ratio between the 660 cm^{-1} peak and the normalized siloxane peak at 1080 cm^{-1} as function of surfactant load. It can be seen that low surfactant concentration induces an increase in the mixed valence oxide phase independently of the alkyl length. The cobalt (II,III) oxide fraction, as calculated by XPS, also demonstrates a similar trend as is shown in Figure 4b. In this case, the fraction of Co_3O_4 is altered as a result of the incorporation of either C2-AB or C6-AB, reaching a maximum of 75% of cobalt as a mixed valence oxide at X=1. By contrast, C12-AB shows a smaller

maximum which occurs at lower surfactant load (X=0.25). Finally, there is suppression of the metal oxide phase with additional surfactant addition (i.e. X>0.25 for C12-AB and X>1 for C2-AB and C6-AB).

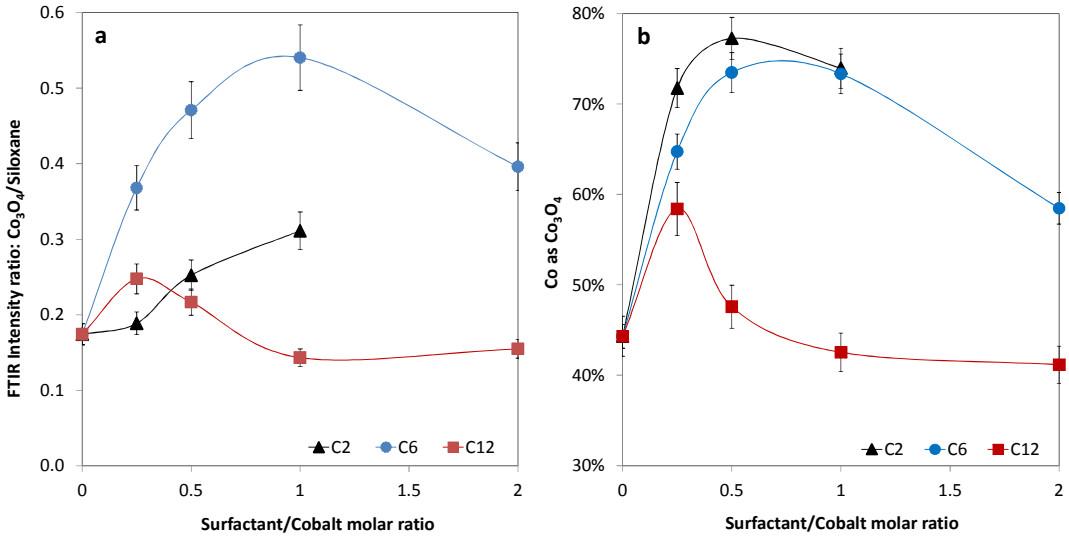

Figure 4: Cobalt oxide evolution as function of surfactant concentration for different alkyl chain lengths: (a) Left: FTIR intensity ratio between cobalt oxide and normalized siloxane peaks. (b) Right: %Co as Co_3O_4 from XPS Co 2p region.

Discussion

The presence of $CoBr_x^{2-x}$ species within all the as-synthesized xerogels facilitates the promotion of Co_3O_4 during heat treatment, bearing in mind that $CoBr_x^{2-x}$ species are formed in equal amounts in each one of the different tested materials regardless of the surfactant used (Figure 3b). In the case of higher surfactant loadings, it has been previously shown that there are additional interactions between $CoBr_x^{2-x}$ species and the increased number of surfactant heads.[16] This in turn reduces the overall amount of Co_3O_4 formed. Interestingly, in this work the decrease in Co_3O_4 occurs at a lower surfactant ratio for the larger C12-AB when compared with both the smaller surfactants, C2-AB and C6-AB (Figures 4a and 4b). These results strongly suggest the larger C12-AB surfactant inhibits the beneficial effect of the Co-Br complex on oxidation.

It is noteworthy to observe that the decline in cobalt (II,III) oxide formation is accompanied by an increase in the mesoporosity for the C12-AB incorporated samples. Indeed, the PSD analysis showed that mesoporosity becomes dominant above X=0.25, corresponding with an abrupt increase in surface area and pore volume (Figure 1c and 1d). The same value (X=0.25) is yields the maximum cobalt oxidation as showed by XPS analysis (Figure 4b). It was previously thought that the mesoporosity was connected with surfactant aggregate formation, whilst the inhibition of cobalt (II,III) oxide formation was connected with additional interactions between the Co-Br complex and the surfactant.[16] However, it now appears that both mechanisms are interconnected.

It is well accepted that aggregation of surfactant within the silica framework is used to tailor pore sizes.[8] As an essential part of the templating mechanism, the contact area between the surfactant and silica surface increases as a result of the aggregation of surfactant monomers.[25,35] In sol-gel derived cobalt silica this may promote intimacy between surfactant and embedded metal species. For instance, the early drop of mixed valence oxide phase on C12-AB samples can be related with the longer tail of C12-AB and lower CMC compared with the other two surfactants (Table 1). In this case C12-AB forms aggregated species at lower concentrations than C6-AB and C2-AB, promoting a faster enlargement of contact area and additional interactions within silica. Therefore, the mesoporous transition and inhibition of cobalt (II,III) oxide formation is simultaneously observed at low surfactant concentration for the C12-AB sample.

The understanding of the inhibition of cobalt (II,III) oxide formation which takes place at high surfactant load can be further elaborated based on this new information. Figure 5 depicts a schematic view of the as-synthesized material and the growing interactions between embedded species as the surfactant load is increased. At low surfactant addition, monomers and cobalt species (Co-Br and other complexes) may take independent contact sites, irrespective of the surfactant alkyl length (Top left and right of Figure 5). Therefore, Co-Br complexes freely contribute to improving the amount of metal that undergoes oxidation as reported in the previous oxidation model.[16] Further

addition ($0.25 < X < 0.5$) of the smallest surfactants (C2-AB and C6-AB) has only minor impacts as the contact sites are filled (Middle left of Figure 5). By contrast, local aggregation of monomers may start in the case of C12-AB (Middle right of Figure 5) due to the stronger hydrophobic forces between free monomers and those already on the surface.[25] Lastly, an excess load of surfactant of any kind ($X > 1$) promotes surfactant aggregation (Bottom of Figure 5) due to surface saturation. These aggregated species facilitate additional interaction between surfactant heads and the nearby Co-Br complexes due to the expansion of the interfacial surface (red dotted line). As reported, these interactions shift the alkyl removal process throughout the thermal treatment into higher temperatures (above 450 °C).[16] Further oxidation of the engaged cobalt is unlikely to form Co_3O_4 due to the unfavourable thermodynamic conditions. Indeed, the equilibrium conversion of $CoBr_2$ toward Co_3O_4 is strongly inhibited at temperatures above 300 °C,[36] thereby diminishing the mixed valence oxide phase formation.

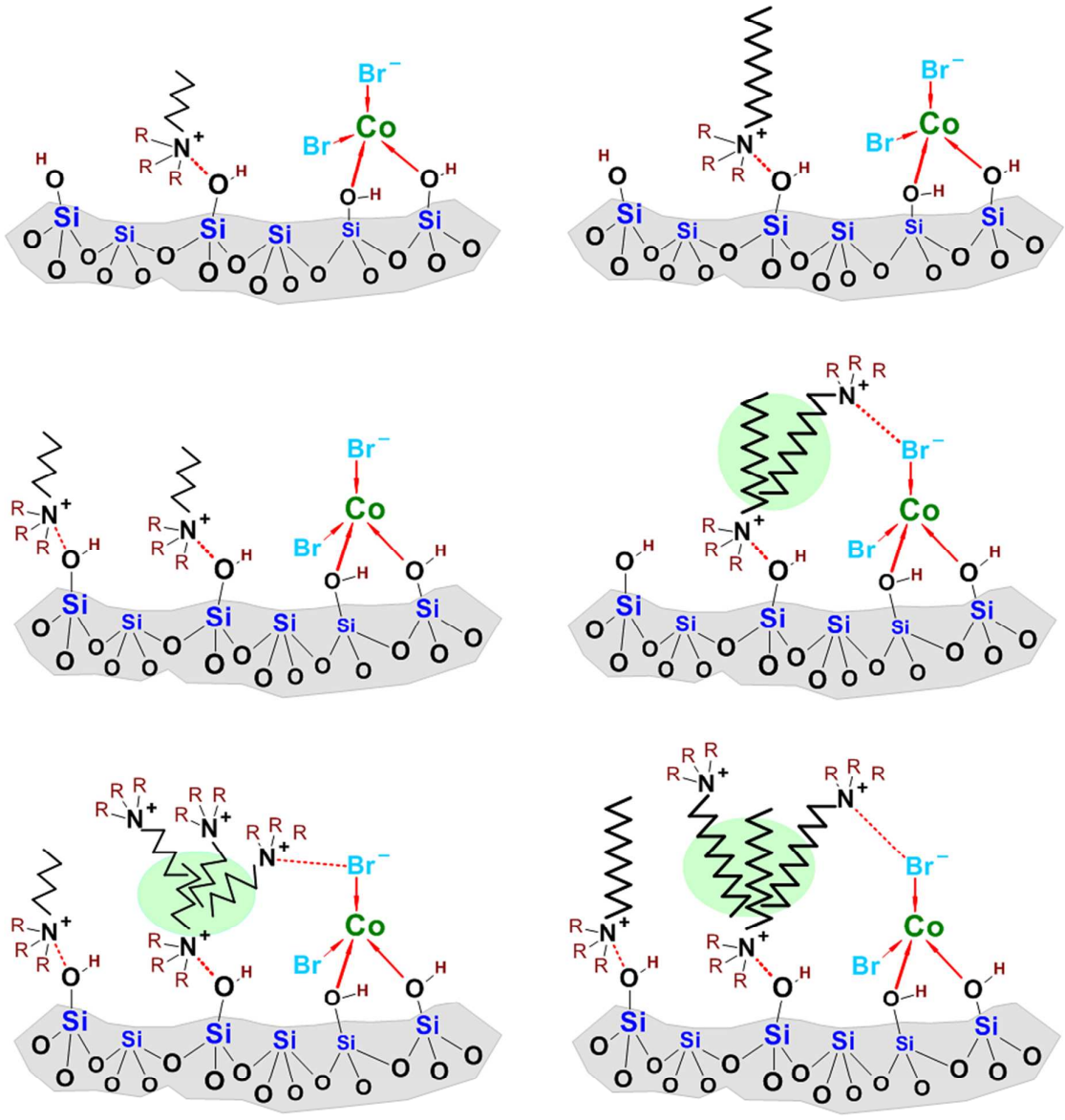

Figure 5: Inhibition of cobalt oxidation. The LEFT sequence represents a small surfactant (C2-AB and C6-AB). The RIGHT sequence represents C12-AB. (Top) At low surfactant load, surfactant monomers take place at independent contact points on the silica surface. (Middle) At moderate surfactant load ($0.25 < X < 0.5$) local aggregation starts only in C12-AB samples (green area) due to stronger hydrophobic forces, hence additional interactions with Co-Br complex emerge. (Bottom) At high surfactant loads ($X > 1$) aggregated species emerge regardless of alkyl length due to surface saturation, promoting additional interactions with Co-Br complexes whereby oxidation is inhibited.

Conclusion

This work shows for the first time that the length of the alkyl chain in cationic surfactants influences both the pore morphology and the metal oxidation state in cobalt oxide silica materials. Importantly, these two mechanisms are apparently interconnected. Addition of C2-AB, C6-AB or C12-AB formed that $CoBr_x^{2-x}$ species in equal amounts regardless of the surfactant used and at low concentrations all surfactants promoted Co_3O_4 formation during thermal treatment of the xerogels. However, as more surfactant is added the enhancement effect is reversed and the cobalt (II,III) oxide content of the sample begins to decline due to increased interactions between the $CoBr_x^{2-x}$ species, the surfactant head groups and the silica surface. The point at which this transition occurs is a function of the alkyl chain length of the surfactant, with a longer chain indicating an earlier transition. The pore size of the silica structure was also influenced by surfactant addition with increasing surfactant loadings promoting mesoporosity. The longer alkyl chain C12-AB surfactant transitioned to a mesoporous pore structure at a lower concentration than either of the smaller C2-AB and C6-AB surfactants. Both the transition to mesoporosity and the peak in cobalt (II,III) oxide content occur at the same surfactant loading strongly suggesting the mechanisms are interrelated. The earlier transition seen in the C12-AB surfactant samples was attributed to the increased propensity of C12-AB to aggregate, given its relatively larger size and lower solubility.

Acknowledgements

The authors would like to acknowledge funding support from the Australian Research Council through Discovery Project Grant DP110101185. Gianni Olguin also acknowledges funding support from the bicentenary scholarship program from the Chilean Government. The authors gratefully acknowledge the technical assistance of Dr Barry Wood of the Australian Microscopy & Microanalysis Research Facility at the Centre for Microscopy and Microanalysis, The University of Queensland.

References

(1) Yacou, C.; Smart, S.; Diniz da Costa, J. C. *Energ. Environ. Sci.* **2012**, *5*, 5820.
(2) Ockwig, N. W.; Nenoff, T. M. **2007**, *107*, 4078.
(3) Liu, L.; Wang, D. K.; Martens, D. L.; Smart, S.; Strounina, E.; Diniz da Costa, J. C. **2014**, *4*, 18862.
(4) Khodakov, A. Y.; Chu, W.; Fongarland, P. *Chem. Rev.* **2007**, *107*, 1692.
(5) Al-Badri, Z. M.; Maddikeri, R. R.; Zha, Y.; Thaker, H. D.; Dobriyal, P.; Shunmugam, R.; Russell, T. P.; Tew, G. N. *Nat. Commun.* **2011**, *2*.
(6) Mattei, G.; Fernandez, C. D.; Mazzoldi, P.; Sada, C.; De, G.; Battaglin, G.; Sangregorio, C.; Gatteschi, D. *Chem. Mater.* **2002**, *14*, 3440.
(7) Cassiers, K.; Linssen, T.; Mathieu, M.; Benjelloun, M.; Schrijnemakers, K.; Van Der Voort, P.; Cool, P.; Vansant, E. F. *Chem. Mater.* **2002**, *14*, 2317.
(8) Wan, Y.; Zhao, D. Y. *Chem. Rev.* **2007**, *107*, 2821.
(9) Duke, M. C.; Diniz da Costa, J. C.; Do, D. D.; Gray, P. G.; Lu, G. Q. *Adv. Funct. Mater.* **2006**, *16*, 1215.
(10) Zou, H.; Wu, S.; Shen, J. *Chem. Rev.* **2008**, *108*, 3893.
(11) Lim, S.; Ciuparu, D.; Pak, C.; Dobek, F.; Chen, Y.; Harding, D.; Pfefferle, L.; Haller, G. *J. Phys. Chem. B* **2003**, *107*, 11048.
(12) Vralstad, T.; Oye, G.; Ronning, M.; Glomm, W. R.; Stocker, M.; Sjoblom, J. *Microporous Mesoporous Mater.* **2005**, *80*, 291.
(13) Katsoulidis, A. P.; Petrakis, D. E.; Armatas, G. S.; Trikalitis, P. N.; Pomonis, P. J. *Microporous Mesoporous Mater.* **2006**, *92*, 71.
(14) Goworek, J.; Kierys, A.; Gac, W.; Borowka, A.; Kusak, R. *J. Therm. Anal. Calorim.* **2009**, *96*, 375.
(15) de Souza, L. K. C.; Pardauil, J. J. R.; Zamian, J. R.; da Rocha, G. N.; da Costa, C. E. F. *J. Therm. Anal. Calorim.* **2011**, *106*, 355.
(16) Olguin, G.; Yacou, C.; Smart, S.; Diniz da Costa, J. C. *Sci. Rep.* **2013**, *3*.
(17) Uhlmann, D.; Liu, S. M.; Ladewig, B. P.; Diniz da Costa, J. C. *J. Membr. Sci.* **2009**, *326*, 316.
(18) Singh, R. D.; Garg, R. *E-J. Chem.* **2010**, *7*, 578.
(19) Gharibi, H.; Razavizadeh, B. M.; Rafati, A. A. *Colloids Surf., A* **1998**, *136*, 123.
(20) Huang, J. B.; Mao, M.; Zhu, B. Y. *Colloids Surf., A* **1999**, *155*, 339.
(21) Li, W.; Han, Y. C.; Zhang, J. L.; Wang, B. G. *Colloid J.* **2005**, *67*, 159.
(22) Corrin, M. L.; Harkins, W. D. *J. Am. Chem. Soc.* **1947**, *69*, 683.
(23) Fuguet, E.; Rafols, C.; Roses, M.; Bosch, E. *Anal. Chim. Acta* **2005**, *548*, 95.
(24) Duke, M. C.; Pas, S. J.; Hill, A. J.; Lin, Y. S.; Diniz da Costa, J. C. *Adv. Funct. Mater.* **2008**, *18*, 3818.
(25) Atkin, R.; Craig, V. S. J.; Wanless, E. J.; Biggs, S. **2003**, *103*, 219.
(26) Lu, Y. F.; Ganguli, R.; Drewien, C. A.; Anderson, M. T.; Brinker, C. J.; Gong, W. L.; Guo, Y. X.; Soyez, H.; Dunn, B.; Huang, M. H.; Zink, J. I. **1997**, *389*, 364.
(27) Raman, N. K.; Brinker, C. J. *J. Membr. Sci.* **1995**, *105*, 273.
(28) Fine, D. A. *J. Am. Chem. Soc.* **1962**, *84*, 1139.
(29) Bobtelsky, M.; Spiegler, K. S. *J. Chem. Soc.* **1949**, 143.
(30) Wertz, D. L.; Kruh, R. F. *Inorg. Chem.* **1970**, *9*, 595.
(31) Martyanov, I. N.; Uma, S.; Rodrigues, S.; Klabunde, K. J. *Langmuir* **2005**, *21*, 2273.
(32) Verberckmoes, A. A.; Weckhuysen, B. M.; Schoonheydt, R. A. **1998**, *22*, 165.
(33) Yang, J.; Liu, H.; Martens, W. N.; Frost, R. L. **2009**, *114*, 111.
(34) Chen, J. F.; Zhang, Y. R.; Tan, L.; Zhang, Y. *Ind. Eng. Chem. Res.* **2011**, *50*, 4212.
(35) Cosgrove, T. *Colloid science: principles, methods and applications*; 2nd ed.; Wiley: Chichester, West Sussex, 2010.

(36) Speight, J. G. *Lange's handbook of chemistry*; McGraw-Hill New York, 2005; Vol. 1.

Supplementary Information

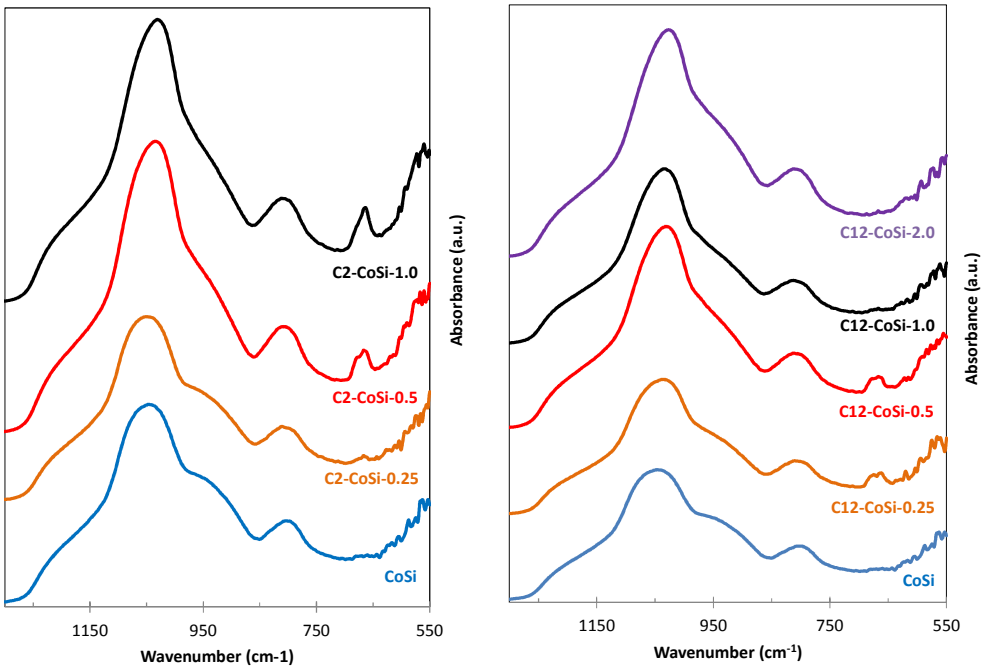

Figure S1: FTIR normalized spectra of calcined xerogels as a function of surfactant concentration. Left: C2-AB. Right: C12-AB. The alteration of the Co_3O_4 characteristic peak at 667 cm^{-1} (Co^{3+}-O vibration) can be observed as surfactant load increases.

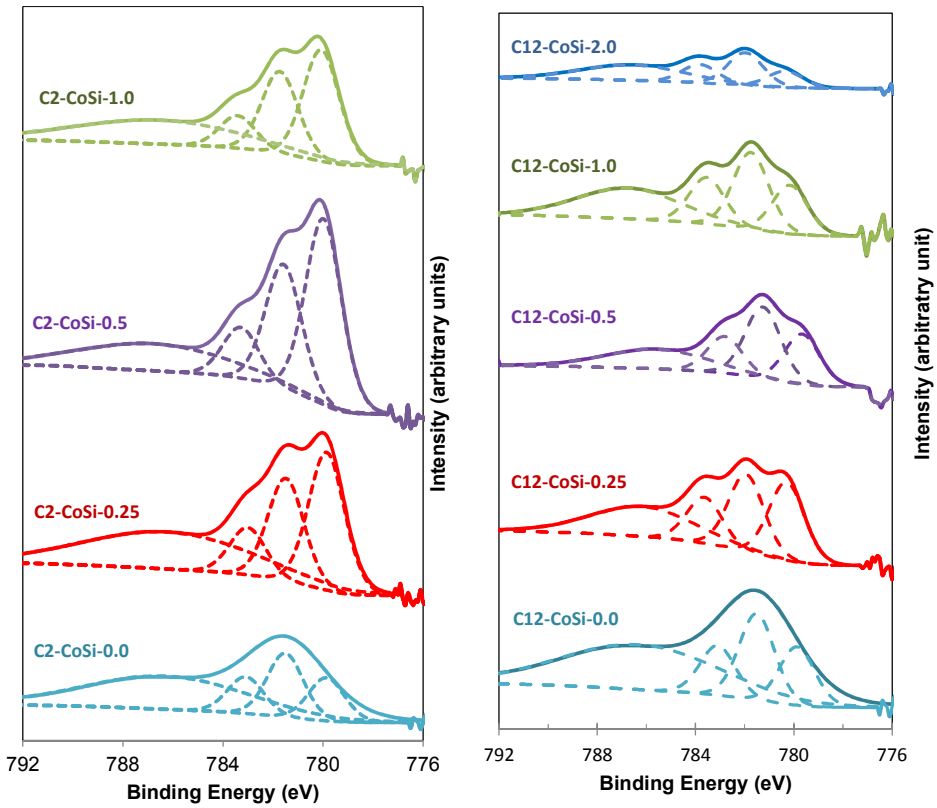

Figure S2: Evolution of XPS spectra near Co2p region for calcined xerogels as function of surfactant concentration. Left: C2-AB. Right: C12-AB. The alteration of the characteristic low energy peak at 779.9 eV which is connected with a high valence state of cobalt, can be observed as surfactant load increases.

Table S1: XPS peak deconvolution data. Peaks position (eV), width, area and goodness of fit for each sample displayed in Figure S2.

Sample	Co^{+3} ($2p_{3/2}$) (fwhm 1.7 eV)		Co^{+2} ($2p_{3/2}$) (fwhm 1.7 eV)		Co^{+2} ($2p_{3/2}$) (fwhm 1.7 eV)		Satellite ($2p_{3/2}$) (fwhm 5-8 eV)		Chi square STD residual
	Position	Area	Position	Area	Position	Area	Position	Area	
CoSi	779.9	757.5	781.6	1126.3	783.2	644.7	786.4	2619.6	0.804
C2-CoSi-0.25	779.9	2420.6	781.5	1808	783.1	831.2	786.3	3070	0.969
C2-CoSi-0.5	779.9	3263.4	781.6	2181.8	783.3	891.1	786.8	2025	0.892
C2-CoSi-1.0	780.0	1957.8	781.7	1441.8	783.4	571.3	786.6	1987	0.756
C12-CoSi-0.25	780.1	265.4	781.8	260.6	783.5	155.8	785.3	375.1	0.795
C12-CoSi-0.5	779.7	170.4	781.3	242.7	782.9	124.1	785.5	195.5	0.864
C12-CoSi-1.0	780.1	632.5	781.7	996	783.5	601.8	786.76	1171.6	0.907
C12-CoSi-2.0	780.1	55.4	781.8	110.4	783.5	62.15	786.4	40.3	0.796

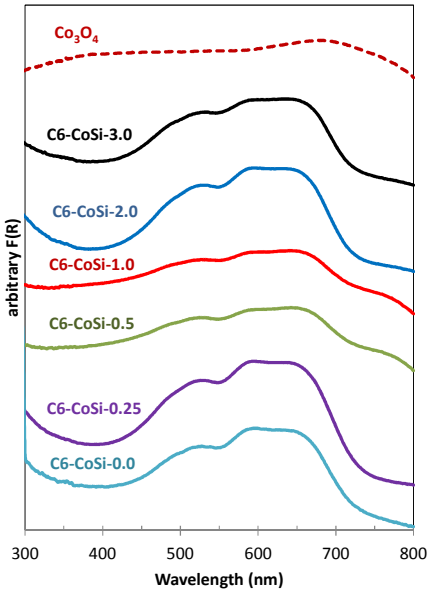

Figure S3: DR-UV Visible spectrum as function of surfactant load for the calcined C6-AB samples and pure Co_3O_4.